journal of the mechanical behavior of biomedical materials 110 (2020) 103914

Contents lists available at ScienceDirect

Journal of the Mechanical Behavior of Biomedical Materials

journal homepage: http://www.elsevier.com/locate/jmbbm

Fiber reorientation in hybrid helicoidal composites

Di Wang [a], Alireza Zaheri [b], Benjamin Russell [b,1], Horacio Espinosa [b,**], Pablo Zavattieri [a,*]

[a] Lyles School of Civil Engineering, Purdue University, West Lafayette, IN, 47907, USA
[b] Department of Mechanical Engineering, Northwestern University, Evanston, IL, 60208, USA

ARTICLE INFO

Keywords:
Hybrid helicoidal composites
Biomimetic nacre/helicoidal composites
Fiber reinforced compliant matrix
Fiber reorientation
Finite element analysis (FEA)

ABSTRACT

Naturally occurring biological materials with stiff fibers embedded in a ductile matrix are commonly known to achieve excellent balance between stiffness, strength and ductility. In particular, biological composite materials with helicoidal architecture have been shown to exhibit enhanced damage tolerance and increased impact energy absorption. However, the role of fiber reorientation inside the flexible matrix of helicoid composites on their mechanical behaviors have not yet been extensively investigated. In the present work, we introduce a Discontinuous Fiber Helicoid (DFH) composite inspired by both the helicoid microstructure in the cuticle of mantis shrimp and the nacreous architecture of the red abalone shell. We employ 3D printed specimens, analytical models and finite element models to analyze and quantify in-plane fiber reorientation in helicoid architectures with different geometrical features. We also introduce additional architectures, i.e., single unidirectional lamina and mono-balanced architectures, for comparison purposes. Compared with associated mono-balanced architectures, helicoid architectures exhibit less fiber reorientation values and lower values of strain stiffening. The explanation for this difference is addressed in terms of the measured in-plane deformation, due to uniaxial tensile of the laminae, correlated to lamina misorientation with respect to the loading direction and lay-up sequence.

1. Introduction

Bio-composites found in the exoskeletons of crustacean and mollusk shells combine stiff mineralized (inorganic) reinforcement with ductile biopolymers (organic) to form complex hierarchical architectures (Chen et al., 2012; Meyers et al., 2008; Zhang et al., 2010). The superior mechanical properties of these protective architectured materials, such as stiffness, strength, and fracture toughness, are of critical importance to the organism survival. This is accomplished in part through the combination of stiff and ductile materials and a hierarchical architecture over a range of length scales. Interestingly, nature offers a broad diversity of architectural motifs, exemplify the multitude of ways in which exceptional mechanical properties can be achieved. Such diversity is the source of bio-inspiration and its translation to synthetic material systems. Indeed, bio-inspired materials made by additive manufacturing technologies display similar deformation mechanisms and superior properties (de Obaldia et al., 2015; Porter et al., 2017; Studart, 2016; Suksangpanya et al., 2018; Yin et al., 2019; Zhang et al., 2016, 2015). On the other hand, metallic layered composites made by sintering exhibit enhanced damage tolerance (Hofer et al., 2020). In this work, we combine two architectures: (i) the "fiber helicoid (or Bouligand)" (Bouligand, 1972; Meyers et al., 2008) and (ii) the "brick and mortar" to investigate, what we will call, *discontinuous fiber helicoids* (DFH), which was first introduced and investigated by Zaheri et al. (2018). As a complement to this previous work, the current paper focuses on the fiber reorientation and its contribution to strain stiffening behavior before failure occurs, which is analyzed via nonlinear micromechanical finite elements. The fiber helicoid is found in the dactyl club of the Peacock mantis shrimp (*Stomatopod*) (Fig. 1(a) and (b)) (Grunenfelder et al., 2014; Guarín-Zapata et al., 2015; Weaver et al., 2012), the cuticle of arthropods (Cheng et al., 2011, 2008; Grunenfelder et al., 2014; Raabe et al., 2005; Sachs et al., 2008; Weaver et al., 2012; Yao et al., 2013; Zelazny and Neville, 1972), fish scales (Bigi et al., 2001; Bruet et al., 2008; Fang et al., 2014; Gil-Duran et al., 2016; Ikoma et al., 2003; Lin et al., 2011; Meyers et al., 2012; Murcia et al., 2017; Torres et al., 2008; Yang et al., 2014, 2019; Zhu et al., 2012; Zimmermann et al., 2013), and plants (Chung et al., 2011; Roland et al., 1989). The brick and mortar is found in sea shells, e.g., the innermost layers of red abalone (Haliotis

* Corresponding author.
** Corresponding author.
E-mail addresses: espinosa@northwestern.edu (H. Espinosa), zavattie@purdue.edu (P. Zavattieri).
[1] Current affiliation: *Engineering Department, University of Cambridge, Cambridge UK*.

https://doi.org/10.1016/j.jmbbm.2020.103914
Received 31 January 2020; Received in revised form 24 April 2020; Accepted 4 June 2020
Available online 24 June 2020
1751-6161/

rufescens) (Barthelat et al., 2016; Ji and Gao, 2004; Menig et al., 2000; Salinas and Kisailus, 2013; Sun and Bhushan, 2012) (Fig. 1(c) and (d)).

While the fracture resistance, toughening behavior and photonic sensory mechanism of helicoid architecture under out-of-plane impact, bending (Ginzburg et al., 2017; Grunenfelder et al., 2014; Mencattelli and Pinho, 2019; Suksangpanya et al., 2018, 2017; Weaver et al., 2012), and uniaxial tensile loading (Zaheri et al., 2018) (Kose et al., 2019; Shishehbor and Zavattieri, 2019) have been extensively investigated, the mechanical behavior of fiber helicoid architectures, prior to failure, have been much less studied. For instance, it has been recently proposed that helicoidal arrays of fibrils, present in *Arapaima Gigas* scales, adapt to the loading environment through laminae rotation towards the loading direction, whereas other laminae, with large off-axis angle, rotate away from the loading direction (Quan et al., 2018; Yang et al., 2014; Zimmermann et al., 2013). As reported by Zimmerman et al. (Zimmermann et al., 2013), this so-called "sympathetic" fiber reorientation has been found to contribute to enhanced ductility and toughness in fish scales (Yang et al., 2019). In the spirit of bio-mimicry, Zaheri et al. (2018) designed a discontinuous fiber helicoidally sample to gain further insight into the phenomenon. Tensile experiments performed on such samples showed features of strain stiffening consistent with large deformation effects. However, detailed modeling accounting for fiber rotation and matrix constitutive response are needed to decouple the two effects and gain insight into the potential of discontinuous fiber helicoidally structures. Among the few models reported in the literature for related phenomenon, we can mention the work by Yang et al. (2017), which formulated a theoretical framework to predict the rotation of two-dimensional hard particles in a soft matrix. However, such model is limited to particles with small aspect ratios and does not incorporate the anisotropic behavior typically found in composite materials. Besides, their model does not consider the rotation of particles in a multilayer laminate. Accordingly, the study of fiber reorientation in laminates with

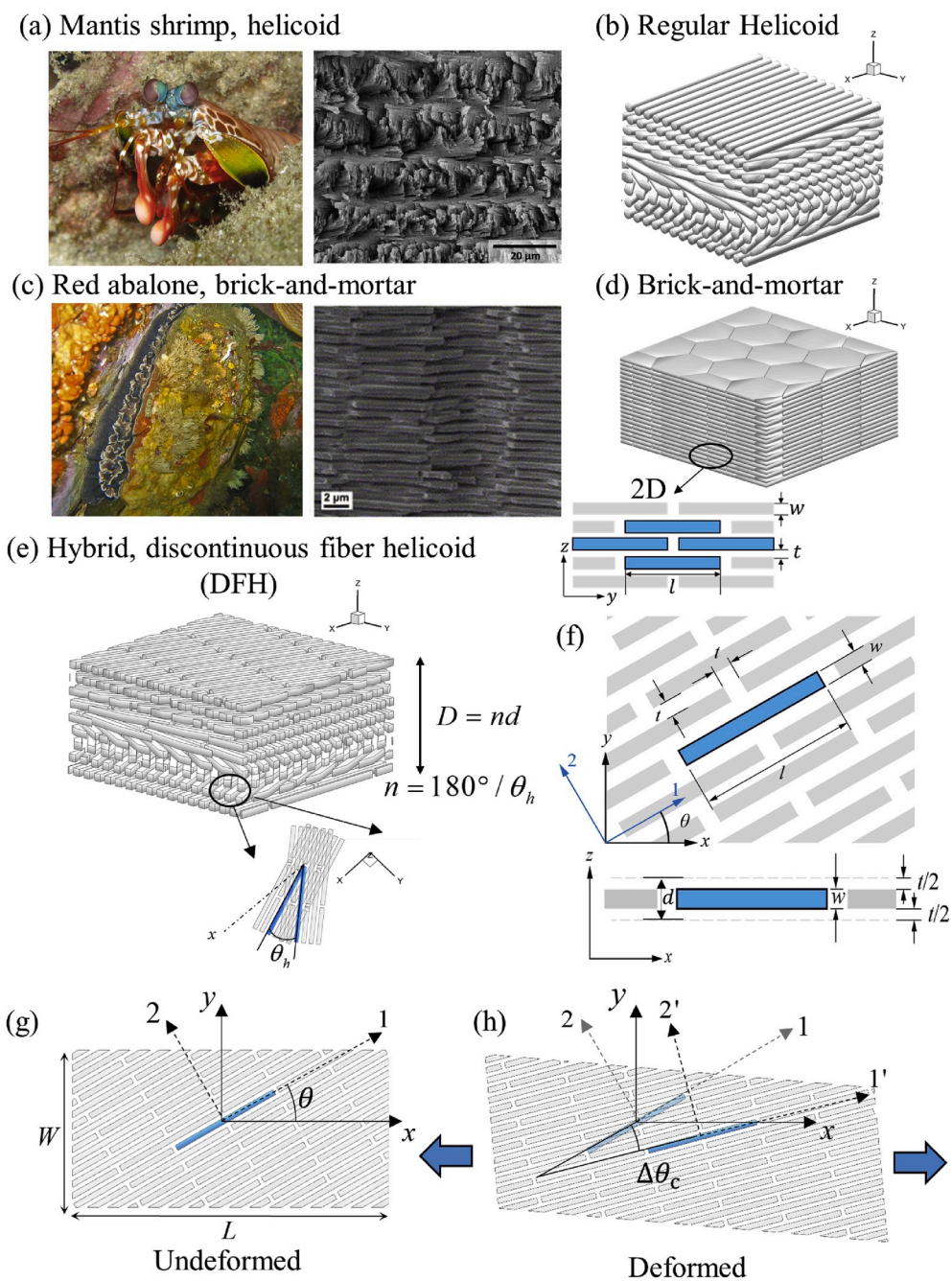

Fig. 1. Biological architectures found in nature: (a) Helicoid architecture of the mantis shrimp dactyl club, and (b) regular helicoid architecture. (c) Biological brick-and-mortar architecture of the red abalone, and (d) regular brick-and-mortar architecture. (e) The discontinuous fiber helicoid architecture (DFH), and (f) Dimensions of the DFH architecture. (g) Undeformed single layer with misorientation θ with respect to the loading axis. (h) Schematic of fiber rotation $\Delta\theta_c$ due to stretch only. Photo credits (a) courtesy of S. Baron with adapted size, under CC by 2.0(left) and adapted from (Grunenfelder et al., 2014) (right); (c) courtesy of Southwest Fisheries Science Center, NOAA Fisheries Service (left) and adapted from (Barthelat et al., 2007) (right).

distinct misaligned angle requires different theoretical and computational treatments.

As illustrated in Fig. 1(e), the DFH architecture consists of aligned and staggered fibers (in the *x*-*y* plane), in which each lamina presents a fiber rotation by a constant pitch angle, θ_h, from the preceding lamina (along the *z*-axis). For example, for $\theta_h = 30^\circ$ the lay-up sequence is [0/30/60/90/120/150], where the angle is defined between the fiber and the *x*-axis. Once the lamina achieves 180° rotation, with respect to laminae with misorientation 0°, a full period in the helicoid architecture is achieved. The number of laminae needed to complete a 180° rotation is $n = D/d = 180^\circ/\theta_h$, where D is the period of the DFH architecture, also called pitch distance (Guarín-Zapata et al., 2015), Fig. 1(e). d is the height of one lamina, composed of fiber height, w, and the separation between two fibers, t, such as $d = w + t$, as shown in Fig. 1(f). Employing this geometry and Finite Element Analysis (FEA), we investigate the fiber rotation and matrix response, for several matrix constitutive laws, to elucidate the origin of strain stiffening in the DFH architecture as a function of imposed deformation (Zaheri et al., 2018). Both nonlinear constitutive response and finite deformations are investigated. To decouple the effects of fiber rotation, Fig. 1(g) and (h), and matrix constitutive response on strain stiffening, linear elastic, hyper-elastic, and elasto-plastic matrix constitutive responses are considered. To decouple the composite lay-up effects on fiber rotation upon uniaxial tensile, we introduce two ancillary architectures: discontinuous single lamina (DSL) and discontinuous mono-balanced (DMB). We expect this analysis to provide information on interlaminar constrains in terms of strain and stress, a key characteristic in composites. The computational study will provide information on strain stiffening measured in the DFH architecture, and insights for the design of bio-inspired composites, with the DFH architecture, exhibiting strain stiffening.

2. Methods

2.1. Geometry of 3D printed discontinuous fiber helicoids

The discontinuous fiber helicoid (DFH) composites are 3D printed with two materials. A stiff polymer (VeroWhite (Stratasys Ltd., 2018)) for the fibers and soft polymer, rubber like (nearly incompressible), materials (TangoPlus (Stratasys Ltd., 2019)) for the matrix, see *section S1* of the supplemental material (SI), following Zaheri et al. (2018). VeroWhite material is more than 3 order of magnitude stiffer than the TangoPlus. On the other hand, TangoPlus is brittle under tension and shear deformation and it shows anisotropic behavior, due to the printing process. The fibers are printed with a square cross-section area to maximize resolution of the 3D printer. The stiff fibers have a length, l, and a square cross-section with width, w (Fig. 1(f)). We choose a fiber aspect ratio $l/w = 20$ for all the cases and a sample gauge length to fiber length $L/l = 2.8$ for $L/W = 2$, which is the aspect ratio of the gauge, see Fig. 1(g). The soft matrix separates the fibers in all three dimensions by a thickness t, as illustrated in Fig. 1(f). The ratio of matrix thickness over the fiber width is also kept constant $t/w = 0.8$ for all the cases. As such, the fiber volume fraction is 29.7%. Further analysis indicates that materials with this fiber volume fraction are sufficient to be considered as a homogeneous anisotropic behavior in each lamina. Within the plane of a single lamina, the fiber and matrix form a brick and mortar structure, where fibers are off-set from neighboring rows by a distance $(l+t)/2$ to provide optimum staggering for shear transfer, Fig. 1 (f). This results in maximum in-plane stiffness in the longitudinal direction (Sakhavand and Shahsavari, 2015; Wei et al., 2012; Zhang et al., 2015, 2010). Each lamina is defined by its misorientation, θ_i, with respect to the loading direction (*x*-direction). Here, the subscript "*i*" refers to the misorientation in a given lamina, Fig. 1(g). For example, θ_{30} represents the lamina with a misorientation of 30° with respect to the loading direction. Any fiber reorientation upon deformation is labeled as $\Delta\theta_c$, as shown in Fig. 1 (h). Further details of specimens and tests are given in (Zaheri et al., 2018).

2.2. FEA model

The FEA model of 3D printed dog-bone samples is depicted in Fig. S1. Geometries are meshed using first order tetrahedral elements (C3D4). The mesh size is selected such that there is mesh convergence (See *section S2)*. Finite deformation is included in all simulations. The fiber material is modeled as linear elastic with a Young's modulus $E = 1.108$ GPa and Poisson's ratio $\nu = 0.3$. The matrix is modeled as a hyperelastic material with a 2nd order polynomial model (Rivlin and Saunders, 1951). The model parameters are obtained by fitting matrix stress-strain experimental results in tensile and shear deformation, see *section S1*. In a subset of simulations, the matrix is also considered to be linear elastic with a Young's modulus $E = 0.337$ MPa and elasto-plastic with a bilinear law with a hardening modulus of 0.03 MPa and a yielding stress of 0.014 MPa.

Most of the numerical simulations are conducted on specimens with finite size and free-edge boundary conditions on the faces with normal vectors in the *y*- and *z*-directions to replicate the conditions during the experiments, Fig. S1 and Fig. S3(c). However, to assess the applicability of these results to architectures with a large number of laminae in the *z*-direction (number of pitches, $N \to \infty$), a set of simulations is carried out with periodic boundary conditions on the planes perpendicular to the *z*-axis. Faces with vector normal in the direction of the *y*-axis remain free. Hence, we denote this configuration by free-periodic boundary condition, see Fig. S3(d). A uniform displacement is prescribed in the *x*-direction, on the loading faces of the specimen, while the faces of the tabs normal to *y*- and *z*-axes are fixed in the *y*- and *z*-directions, Figs. S3(c–d), for both free-free and free-periodic boundary conditions.

Fiber reorientation in each individual lamina is directly extracted from the FEA by computing the average rigid body rotation in each fiber. The simulations reveal that fiber rotation induced by stretch only, $\Delta\theta_c$, is hindered by the rotation of the gauge section. Thus, in addition to the rotation that arises through stretching, rotation of the gauge section of the specimen (warping effect) also contributes to the apparent rotation. The latter contribution is removed since this is a geometric effect related to the fiber initial orientation, dimensions of the specimen, boundary condition, and the number of periodic layers. In the calculations, the warping effect is removed by polar decomposition of the deformation gradient. Details of the calculation process are provided in *Section S3*.

2.3. Analytical model

While limited to small strains, analytic methods can be used to obtain homogenized properties for both single oriented lamina and laminate composed of multiple laminae. Here, we employ the Halpin-Tsai equation (Halpin, 1969; Tucker and Liang, 1999) to predict the elastic modulus of each layer with staggered-discontinuous fibers. Since Halpin-Tsai requires scalar quantities for the moduli, inputs are obtained through linearization of the matrix material under uniaxial tensile. The Halpin-Tsai equation for moduli is give as:

$$\frac{P}{P_m} = \frac{1 + \xi\eta v_f}{1 - \eta v_f} \; with \; \eta = \frac{(P_f/P_m) - 1}{(P_f/P_m) + \xi}, \tag{1}$$

where, P represents one of the homogenized composite moduli, such as E_{11}, E_{22} and G_{12}. P_f and P_m are the fiber and matrix moduli, respectively. ξ is an empirically derived factor that depends on the boundary conditions. For the quantities E_{11}, E_{22} and G_{12}, the factor ξ takes the values: $2(l/w)$, 2 and 1, respectively. Classical Laminate Plate Theory (CLPT) (Daniel and Ishai, 1994; Ramirez, 1999) is used for predicting the in-plane stiffness of a complete laminate.

3. Results and discussion

3.1. Stress-strain response of hybrid helicoids

The experimental stress-strain response of the 3D printed DFH architecture with various pitch angles θ_h shows a complex behavior as it can be observed in a typical stress-strain response in Fig. 2(a) (Case $\theta_h = 30°$). The complete set of experimental data and FEA data for θ_h in the range 30°-90° is given in section *S4*. The stress-strain response for all DFH architectures can be divided into 3 distinct regions, Fig. 2(a). Region I is defined by an initial elastic response with modulus E_{ini}. Region II shows a drop in the tangent modulus associated with fiber-matrix debonding at the fiber ends, followed by a hardening response. In this region a minimum and maximum tangent modulus can be defined, E_{min} and E_{max}, respectively, details described in *section S5*. Likewise, we can define a stiffening parameter defined as the ratio of $\Gamma = E_{max}/\ E_{min}$. Region III describes the material response as it accumulates further damage followed by final failure (Zaheri et al., 2018).

3.2. Moduli and strain stiffening

In our FEA, Regions I and II are independently considered to study the behavior of laminates without and with local discontinuity in the matrix between fiber ends, see *section S6*. The purpose of the first set of simulations is designed to capture the initial modulus E_{ini} (Region I with intact matrix), while the second set of simulations includes discontinuities at the ends of the fibers (*debonded fiber-matrix interface*) to capture the stress-strain behavior in Region II. The second set of models is also employed to compute the stiffening parameter Γ. Specifically, in the FEA with discontinuous matrix (Region II), the elastic modulus after accumulated deformation is defined by E_{max} and the elastic modulus at the beginning of the stress and strain curve is defined by E_i. Hence, $\Gamma_{iof} =$

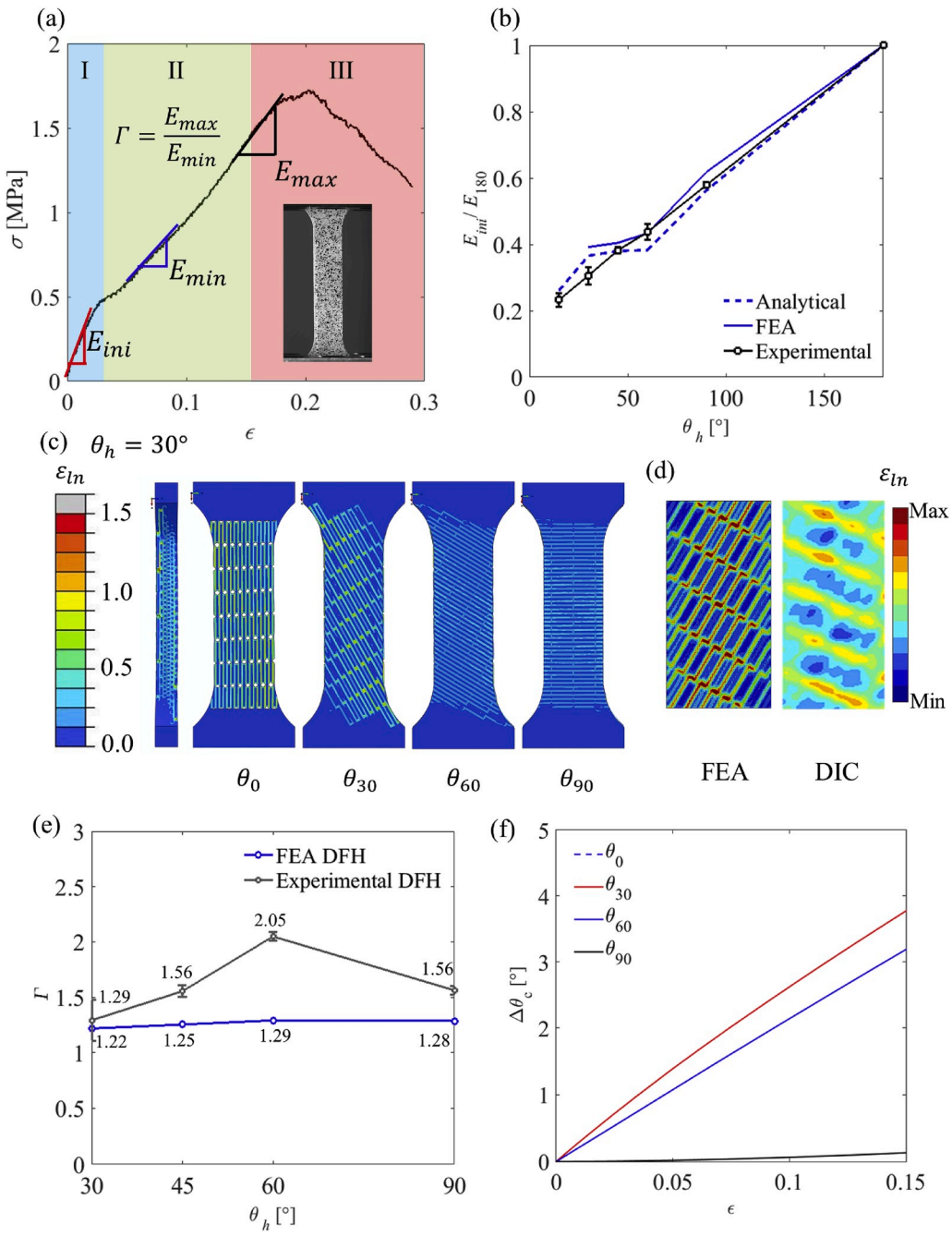

Fig. 2. (a) Experimental stress and strain curve of DFH $\theta_h = 30°$ with $L/W = 2$ and definition of elastic modulus in three regions. (b) Initial elastic modulus, E_{ini}, normalized by the elastic modulus of the lamina with misorientation 0° with respect to the loading direction, E_{180}, as a function of pitch angle, θ_h. (c) Contour plot of maximum principal logarithmic strain, ε_{ln}, as predicted by FEA, lamina by lamina. (d) FEA predictions and experimental measurements (DIC) of maximum principal logarithmic strain, ε_{ln}, in the θ_{30} lamina of the DFH with pitch $\theta_h = 30°$. (e) Γ as a function of θ_h calculated from FEA prediction with the hyperelastic matrix when applied strain, ε, is 15%, compared with Γ calculated from experimental stress and strain curves (Zaheri et al., 2018). (f) Fiber reorientation due to stretch only, denoted by $\Delta\theta_c$, as a function of applied strain, ε, of individual laminae.

E_{max}/E_i defines the stiffness ratio, which is a measure of strain stiffening. Further details on these parameters can be found in *section S5* with the difference between Γ_{iof} and Γ depicted in Fig. S8(a). The longitudinal elastic modulus of lamina with misorientation 0° , θ_0 or θ_{180}, denoted by E_{180}, are obtained following the Halpin-Tsai equation. Then using the CLPT model, the laminate properties are estimated as depicted in Fig. 2 (b). The employed constituent properties for the fiber are $E = 1108$ MPa, $\nu = 0.3$ and for the matrix $E = 0.337$ MPa, $\nu = 0.48$. The model predicted a lamina longitudinal elastic modulus of 6.07 MPa and a transverse modulus of 0.76 MPa.

The analytical, experimental, and FEA predictions of E_{ini} are in close agreement, as it can be observed in Fig. 2(b). Since the FEA analysis uses a hyperelastic model for the matrix, while the analytical predictions are based on linear elasticity, the agreement is consistent with the isotropic constitutive model. Unlike $\theta_h = 0°$, the DFH architectures with different pitch angles, θ_h, provide more compliant in-plane behavior. Note that some differences between theory/FEA and experimental measurements are apparent when θ_h is smaller than 45°. This maybe partially induced by the distinct components of extensional-bending coupling in the tested asymmetric laminate.

The maximum logarithmic strain distributions for the DFH with $\theta_h = 30°$ obtained from the FEA are plotted lamina-by-lamina in Fig. 2(c). We can observe that the logarithmic strain is distributed evenly in the matrix along the gauge section, which implies finite sample size effects can be neglected. According to the strain distribution at the top surface of the DFH $\theta_h = 30°$, both FEA and experimental results display large strains in the region between fiber ends (red color), Fig. 2(d). Less prominent matrix strains between parallel fibers are also observed (blue color), up to 25% lower than the matrix strains between fiber ends.

3.3. Mechanisms giving rise to strain stiffening

As discussed before, region II of the stress-strain curve is characterized by a strain stiffening behavior, i.e., $\Gamma > 1$. A comparison between experiments and FEA predictions is shown in Fig. 2(e). We note that the FEA results exhibit a similar trend as that measured in experiments, both achieving a maximum value for $\theta_h = 60°$, although the strain stiffening is less prominent in FEA since the 3D printed matrix material employed in the experiments exhibits a slightly different behavior at large strains. We surmise that the difference between FEA and experiments in terms of absolute values of Γ is due to the 3D printed material for matrix. While our model assumes isotropic behavior, the 3D printed material is anisotropic. The detailed explanation and comparison between experiment and FEA is addressed in *section S1* (See. Fig. S2 for example). Besides, the reason why $\theta_h = 60°$ shows the largest difference on Γ can be explained by the fact that the individual layer $\theta = 60°$ in $\theta_h = 60°$ undergoes significantly more global transverse contraction than the individual layer $\theta = 60°$ in $\theta_h = 30°$, for instance. Therefore, there is more local shear deformation between fibers in the matrix leading to a larger strain stiffening. On the other hand, a likely source for such stiffening is fiber reorientation towards the loading direction, as hypothesized by Zimmermann et al. (2013). Hence, we quantify fiber reorientation caused by stretching, $\Delta\theta_c$, in the DFH with $\theta_h = 30°$ by tracking the coordinate of the individual fibers in each lamina in their undeformed and deformed configurations. The averaged fiber reorientation values as a function of strain and fiber orientation in each lamina are plotted in Fig. 2(f), where positive value indicating that fibers rotating toward the loading direction. It is observed that $\Delta\theta_c$ of laminae with small misorientation, such as θ_{30} and $\theta_{150} = \theta_{-30}$, shows higher values than the laminae with larger misorientation, such as θ_{60} and $\theta_{120} = \theta_{-60}$. Moreover, the $\Delta\theta_c$ for fibers along θ_0 and θ_{90} is close to 0 as expected. Indeed, the motion of fibers along θ_0 and θ_{90} is translation in the loading direction despite the significant mismatch of mechanical properties between fiber and matrix. Plots of $\Delta\theta_c$ as a function of applied strain for the DFH architecture with various fiber to matrix moduli ratios, in the range of 0.01–3000, are given in *section S7*. Clearly, softer matrices result in a more prominent reorientation of the fibers towards the loading direction.

While our FEA shows the presence of fiber reorientation in each lamina of the DFH architecture, the effects of the composite lay-up sequence, the occurrence order of lamina misorientation from bottom to top in one laminate, and matrix constitutive response need to be fully understood to ascertain its impact. For example, a hyperelastic matrix response may also lead to strain hardening. Likewise, it is useful to compare the DFH architecture with other architectures such as discontinuous single lamina (DSL) and discontinuous mono-balanced laminate (DMB). The DSL architecture simply comprises one lamina with one misorientation with respect to the loading axis, and the DMB architecture consists of balanced pairs of laminae, where every positive orientation is adjacent to its negative counterpart, shown in Fig. 3(a). In a sense, the DSL architecture configuration avoids interlaminate incompatibilities in terms of deformation. Conversely, the DMB architecture exhibits a simplified lay-up sequence, with one absolute misorientation (see Fig. 3(a)). By contrast, the DFH architecture presents a mixture of different misorientations. Simply stated, the DSL architecture provides an example of unconstrained rotational behavior, while the DMB architecture exhibits a symmetrically constrained configuration, which can be compared to rotations observed in the DFH architecture. To some extent, this allows us to extract information about the fiber reorientation effect as a function of lay-up sequence.

3.3.1. Role of fiber reorientation

We start by comparing analytic predictions of E_{ini} for the DSL and DMB architectures. As depicted in Fig. 3(b), both architectures exhibit the same E_{ini} when $\theta_i = 0°$ and for a range of θ_i between 56° and 90° . The DMB architecture exhibits a greater stiffness than the DSL architecture with misorientations between 0° and 56°. This is due to the reduced contribution of the shear deformation due to the restriction imposed by the adjacent laminae misorientation in the DMB architecture.

Another interesting observation, which could influence the contribution of fiber reorientation to strain stiffening, is that the relation between lamina misorientation, θ_s, and E_{ini} is not linear, as shown in Fig. 3 (b). For instance, even if fibers in $\theta_s = 60°$ rotate 20° toward the loading direction, reoriented at 40° , the stiffening effect would be much less than the stiffening effect of $\theta_s = 30°$ rotating 10° toward the loading direction. FEA are included in Fig. 3(b) for comparison purposes. As it can be observed, the FEA predictions are in good agreement with the analytical results. For the DMB case, the free-periodic boundary condition makes only a small difference on E_{ini} with respect to DMB architecture with free-free boundary.

We next analyze fiber reorientation and define fibers rotating toward the loading direction as positive and away as negative, as illustrated in Fig. 4(a) and (b). Fig. 4(c) shows the stretching-induced rotation, $\Delta\theta_c$, in the DFH architecture alongside rotation in the DMB and DSL architectures. Each point in the figure represents the mean value of $\Delta\theta_c$ in the corresponding lamina and the error bar is defined by the standard deviation among fibers in each lamina. It is observed that the $\Delta\theta_c$ values of each lamina in the DFH architecture are smaller than the ones obtained with the DSLs, up to 29.5% difference. Thus, the fibers in one lamina without constraint from other laminae have more freedom to rotate under uniaxial tensile. The DMB architecture with $\theta_b = 30°$, $\theta_b = 45°$, and $\theta_b = 60°$ shows generally higher $\Delta\theta_c$ values than those in the DFH architecture with $\theta_h = 30°$, $\theta_h = 45°$, and $\theta_h = 60°$. The maximum difference in $\Delta\theta_c$ between the DMB and the DFH architectures is observed between the individual layer θ_{45} in $\theta_b = 45°$ and $\theta_h = 45°$, which is 28.6%.

Different lay-up sequences promote distinct in-plane mechanical properties, such as Poisson's ratio and coupling coefficients, which in turn influences deformation of each lamina and reorientation of fibers embedded in the matrix. Here we discuss the histogram of $\Delta\theta_c$ in

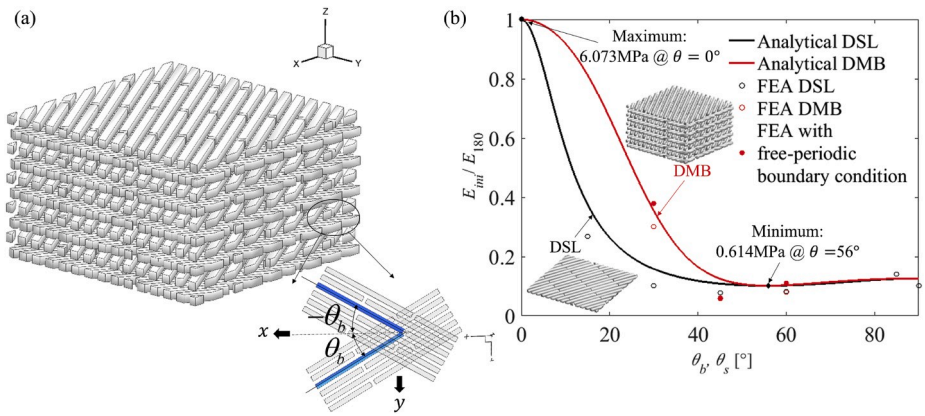

Fig. 3. (a) DMB architecture with absolute misorientation θ_b. Comparison of (b) Normalized FEA and analytical results of DSL and DMB architectures, all with linear elastic matrix.

different architectures, see Fig. 4(d), which depicts the difference of distribution of fiber reorientation among distinct laminates. It is observed that the distribution of $\Delta\theta_c$ in $\theta_s = 30^\circ$ is concentrated between 5° and 6°, while fibers along θ_{30} of the DFH architecture with $\theta_h = 30^\circ$ shows its $\Delta\theta_c$ values between 3° and 5°. However, $\Delta\theta_c$ in the DMB architecture with $\theta_b = 30^\circ$ exhibits increasing fiber amounts with growing $\Delta\theta_c$, which could be partially explained by the specific contraction that DMB architecture undergoes.

The direct correlation between fiber reorientation and stiffness variation is obtained by using a semi-analytical method. E_i can be obtained by considering the lay-up sequence, before deformation, in the CLPT model, and then calculated as $1/h\overline{S_{11}}$, where h is the height of the laminate and $\overline{S_{11}}$ is the in-plane component of compliance matrix in the first row and first column. An averaged fiber reorientation can be obtained by computing the angle between fiber orientations before and after deformation from the FEA. Next, the new deformed lay-up sequence is calculated by using the initial fiber orientation to subtract the averaged fiber reorientation values, when the initial fiber orientation is less than or equal to 90°. When the initial fiber orientation is larger than 90°, we consider sum of the initial fiber orientation and fiber reorientation values as new deformed fiber orientation. E_{max} can then be computed by the new deformed lay-up sequence combined with CLPT. The calculation procedure is the same as the one used for E_i. Finally, the values of Γ_{iof} of $\theta_b = 30^\circ$, 60° and $\theta_s = 0^\circ$, 30, 60°, 90° (associated laminae of the DFH $\theta_h = 30^\circ$) are shown in Fig. 4(e) in comparison with DFH architecture with $\theta_h = 30^\circ$.

The bar chart shows that DMB $\theta_b = 30^\circ$ and DSL $\theta_s = 30^\circ$ stiffen more than the DFH architecture with $\theta_h = 30^\circ$, up to 30.4%, under the same uniaxial tensile stretch. Other laminates, $\theta_s = 0^\circ$, 60°, 90° and $\theta_b = 60^\circ$, show negligible stiffening, compared with $\theta_s = 30^\circ$ and $\theta_b = 30^\circ$. This could be explained by the trends shown in Fig. 3(b), in which no strain stiffening is expected once θ_s is larger than 56°, unless very large $\Delta\theta_c$ occur. Thus, based on these observation, it is possible to conclude that the reason why the DFH architecture with $\theta_h = 30^\circ$ exhibits lower stiffening (Γ_{iof}) is because it shows smaller values of $\Delta\theta_c$ in each lamina, when compared to corresponding lamina misorientation in DSL ($\theta_s = 30^\circ$ and $\theta_s = 60^\circ$) and DMB ($\theta_b = 30^\circ$ and $\theta_b = 60^\circ$) architectures.

3.3.2. Explanation on fiber reorientation based on mechanism

We now look into potential mechanistic explanations on fiber reorientation and its contribution to strain stiffening based on the anisotropic behavior of the different laminae and their individual in-plane shear and transverse contraction deformation induced by the uniaxial load. Using the polar decomposition method, an analytical expression for $\Delta\theta_c$ as a function of in-plane components of the stretch tensor, $\boldsymbol{U}$, can be derived. Consider a unit vector describing fibers in the undeformed configuration with orientation, θ, namely, $\overline{v_0} = (cos\theta,\ sin\theta)$. If $\overline{v}$ is the vector in the deformed configuration, $\overline{v}$ and $\overline{v_0}$ are related by $\overline{v} = \boldsymbol{U}\cdot\overline{v_0}$ (Reddy, 2013) with the angle between them given by $cos\Delta\theta_c = \frac{\overline{v}\cdot\overline{v_0}}{|\overline{v}||\overline{v_0}|}$, or

$$\Delta\theta_c = \arccos\left\{\frac{\left[cos^2\theta U_{xx} + sin^2\theta U_{yy} + 2sin\theta cos\theta U_{xy}\right]}{\sqrt{\left(U_{xx}cos\theta + U_{xy}sin\theta\right)^2 + \left(U_{xy}cos\theta + U_{yy}sin\theta\right)^2}}\right\} \tag{2}$$

where U_{xx}, U_{yy}, and U_{xy} are the in-plane components of the $\boldsymbol{U}$. A close examination of Fig. S5(b) reveals that the theoretical prediction of $\Delta\theta_c$ is in close agreement with the results obtained by FEA and those calculated from whole laminate deformations. A color map of $\Delta\theta_c$ as a function of the individual stretch tensor components can be constructed using Eq. (2), as shown in Fig. 5(a). Moreover, the $\Delta\theta_c$ of each individual lamina for various architectures can be analyzed based on the components of the stretch tensor obtained from simulations. For example, the $\Delta\theta_c$ of the individual lamina θ_{30} in the DMB $\theta_b = 30^\circ$ (shown as a red dot in left-top corner of the color map in Fig. 5(a)) implies that transverse contraction, rather than in-plane shear deformation, U_{xy}, is the one promoting fiber reorientation in the architecture. This result is consistent with the prediction of the CLPT model for balanced architecture, in which the extensional-shear coupling components are zero, i.e., no in-plane shear deformation due to uniaxial tension(Carlsson et al., 2014). By contrast, the $\Delta\theta_c$ of the DSL with $\theta_s = 30^\circ$ (shown as a black dot in Fig. 5(a)) primarily results from U_{xy}, 8.15 times higher than the U_{xy} value of θ_{30} in DMB $\theta_b = 30^\circ$, and moderately results from transverse contraction, U_{yy}, 42.2% lower than the one of DMB architecture. Interestingly, when comparing the DMB architecture to the DSL $\theta_s = 30^\circ$, the former exhibits a 93.4% higher value of the effective Poisson's ratio, ν_{xy}, see Fig. 5(b). The DFH architecture exhibits a behavior in which both in-plane shear deformation and transverse contraction are smaller, blue dot in Fig. 5(a). Less shear deformation than corresponding DSL architectures is because in the DFH architecture, for each lamina with misorientation θ, there is always a lamina with misorientation $-\theta$. Accordingly, at the laminate level, the DFH architecture also satisfies the balanced laminate condition, which means no in-plane shear deformation due to uniaxial tension. On the other hand, unlike the DMB architecture composed of multiple laminae with one absolute value of misorientation, indicating compatible properties lamina by lamina, the DFH architecture is composed of multiple laminae with different absolute values of misorientation, which means incompatible properties lamina by lamina. Therefore, the DFH architecture cannot reach as high transverse contraction as the DMB architecture, and then the individual lamina with different θ in the DFH architecture will rotate less than the corresponding DSL and DMB architectures, see Fig. 5(b) and Fig. S7. The global deformation of the DFH, DMB, and DSL architectures is illustrated in Fig. 5(c–f) and the deformation magnitudes of the different

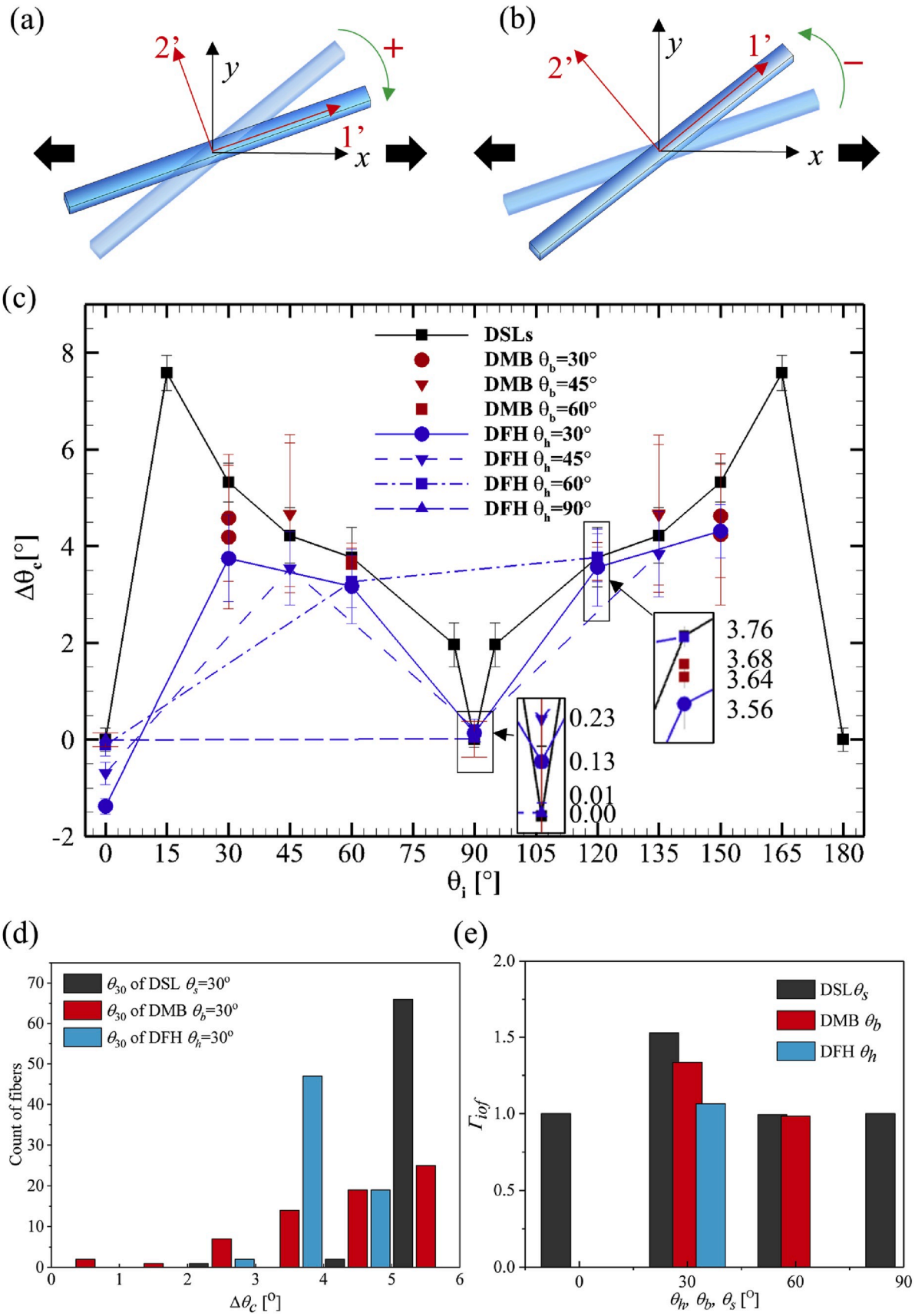

Fig. 4. (a)–(b) Definition of direction on fibers rotation. Positive means fibers rotate toward the loading axis, whereas negative means fibers rotate away from the loading direction. The *x*-axis is the loading direction. 1′ and 2′ axes are local axes after deformation. (c) Fiber reorientation due to stretch only, $\Delta\theta_c$, of individual lamina in DFH/DMB/DSL architectures under 10% local uniaxial strain (15% ε). (d) Histogram of $\Delta\theta_c$ in lamina θ_{30} (e) Semi-analytical Γ_{iof} calculated based on $\Delta\theta_c$ in DFH $\theta_h = 30^\circ$ /DMB/DSL architectures under 10% local uniaxial strain (15% ε).

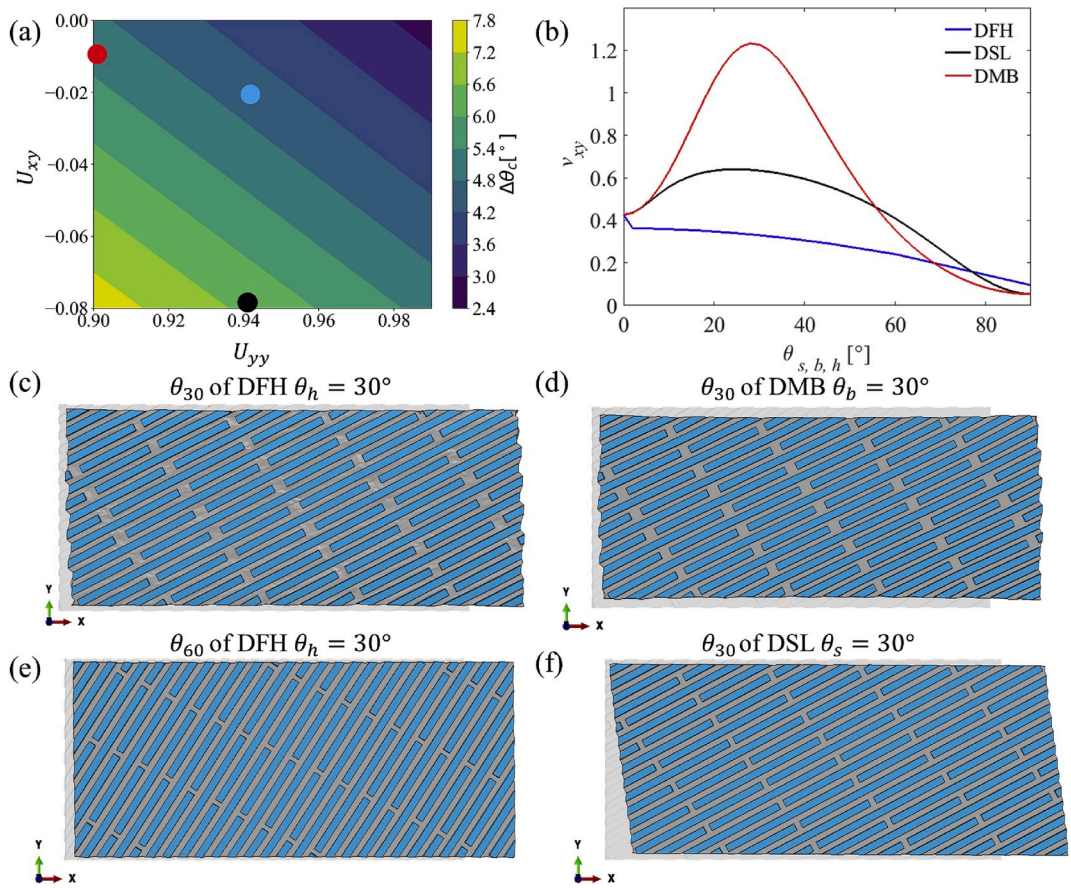

Fig. 5. (a) Color map of $\Delta\theta_c$ as a function of U_{xy} and U_{yy}, where the red dot represents for the lamina θ_{30} in DMB $\theta_b = 30°$, the black dot represents for the lamina DSL $\theta_s = 30°$, and the blue dot represents for the lamina θ_{30} in DFH $\theta_h = 30°$ (b) Poisson's ratio ν_{xy} as a function of θ_s, θ_b and θ_h (c) Configuration of individual lamina θ_{30} in DFH $\theta_h = 30°$ (d) Configuration of individual lamina θ_{30} in DMB $\theta_b = 30°$ (e) Configuration of individual lamina θ_{60} in DFH $\theta_h = 30°$ (f) Configuration of individual lamina θ_{30} in DSL $\theta_s = 30°$, before (light grey) and after deformation (darker grey for matrix and blue for fibers).

architectures, under the same uniaxial tensile strain, are tabulated in Table S1.

3.3.3. Role of matrix mechanical behavior

In the previous section, we studied the correlation between $\Delta\theta_c$ and strain stiffening, Γ_{iof}, by using a semi-analytical method and examining the $\Delta\theta_c$ distribution computed for different architectures. In this section, we investigate the effect of matrix constitutive behavior on strain stiffening. We begin by analyzing a linear elastic matrix and conclude with the analysis of an elasto-plastic matrix.

In analyzing the effect of a linear elastic matrix, a maximum local true strain $\varepsilon_t = 4\%$ is used for comparing various laminates. The local strain is based on the deformation at two ends of the gauge region, u_{gauge}/L_{gauge} whereas the global(applied) strain, ε, is calculated by the applied deformation at the end of dog-bone sample, $u_{applied}/\ L_{gauge}$. A free-periodic boundary condition is applied to all FEA in this section. Moreover, it is important to note that the fiber reorientation values for the DFH and the DMB architectures with linear elastic matrix are the same as the fiber reorientation values computed for the DFH and the DMB architectures with hyperelastic matrix, see *section S8*.

The normalized elastic modulus, along various orientations, for the $\theta_h = 30°$ and $\theta_b = 30°$ architectures, at $\varepsilon_t = 1\%$ ($E_{LE1\%}$), and at 4% ($E_{LE4\%}$), are plotted in Fig. 6(a). By contrast, FEA and analytical predictions are in close agreement for the DMB architectures, 3.95% difference for $\theta_b = 30°$ in both longitudinal and transverse directions. The normalized elastic modulus for the DFH architecture with $\theta_h = 30°$, for both $E_{LE1\%}/E_{180}$ and $E_{LE4\%}/E_{180}$ are smaller than the analytical prediction. This is the case, because in the FEA, the DFH architecture is modeled by discontinuous fibers, resulting in localized failure (fiber end-matrix debonding). As expected, the DFH architecture presents close to in-plane isotropic behavior on elastic modulus, whereas the $E_{LE1\%}$ of $\theta_b = 30°$ is relatively large only in the direction close to the initial lamina misorientation 30° . The value of $E_{LE1\%}$ of the $\theta_b = 30°$ along the longitudinal direction is three times and a half over the value of $E_{LE1\%}$ in transverse direction.

We next examine $\Gamma_{iof(4\%)}$, where $\Gamma_{iof(4\%)}$ is defined as the strain stiffening of architecture finally deformed under 4% of ε_t in uniaxial direction (subscript "4%" means 4% of ε_t), and $\Gamma_{iof(\varepsilon_t)} = E_{max}(\varepsilon_t)/E_i$, value E_{max} as a function of ε_t over E_i. In Fig. 6(c), although $\theta_b = 45°$ shows the maximum $\Delta\theta_c$ and strain stiffening $\Gamma_{iof(4\%)} = 1.16$, compared with $\theta_b = 30°$ and $\theta_h = 30°$, the $E_{LE1\%}$ of $\theta_b = 45°$ is only 18.8% of the value of $\theta_h = 30°$ both in the longitudinal and transverse directions. Although a small stress softening value ($\Gamma_{iof(4\%)} = 0.92$) is exhibited by the DFH architecture, isotropic stiffness is achieved.

It is important to understand if the specific lay-up sequence of the DFH architecture can influence $\Delta\theta_c$ and strain stiffening and thus, we consider a disorder laminate $\theta_r = [30/150/60/120/0/90/30]$, which contains the same associated laminae but different lay-up sequence from $\theta_h = 30°$. θ_r is representative of other alternative laminates with different lay-up sequences, since E_i calculated by CLPT is independent on the lay-up sequence, shown in *section S9*. In Fig. 6(b), the elastic modulus of disorder laminate θ_r before and after deformation, compared with $\theta_h = 30°$, is shown. It is observed that the values of E_i of θ_r and $\theta_h = 30°$ show close agreement on both analytical prediction and FEA. However, the $\Gamma_{iof(4\%)}$ of θ_r due to difference on fiber reorientation is 1.44% higher than the value of $\theta_h = 30°$, as depicted in Fig. 6(d). This

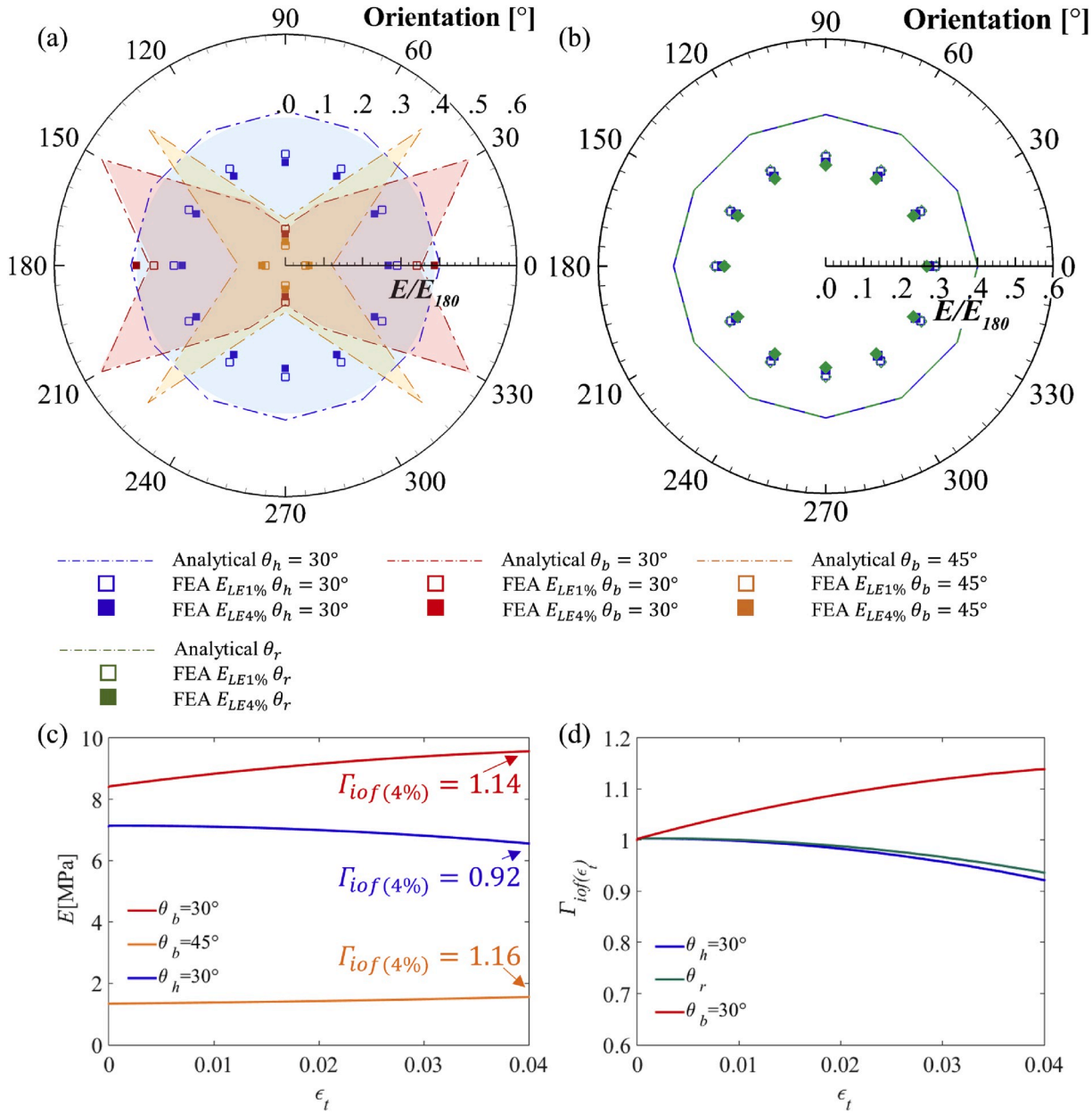

Fig. 6. FEA predictions on elastic modulus of laminates with linear elastic matrix deformed within 1% local true strain, ε_t, ($E_{LE1\%}$) and at ~4% ε_t ($E_{LE4\%}$). Analytical predictions are based on the CLPT model. (a) Comparison among $\theta_h = 30^\circ$, $\theta_b = 30^\circ$ and $\theta_b = 45^\circ$ (b) Comparison between $\theta_h = 30^\circ$ and the disorder architecture with lay-up sequence [30/150/60/120/0/90/30] (c) Elastic modulus as a function of local true strain, ε_t. (d) Stiffening parameter $\Gamma_{iof(\varepsilon_t)}$ as a function of ε_t.

means that different lay-up sequence does influence the stiffness variation caused by fiber reorientation. However, compared with the strain stiffening $\Gamma_{iof(\varepsilon_t)}$ of the DMB $\theta_b = 30^\circ$, Fig. 6(d), the difference between θ_r and DFH $\theta_h = 30^\circ$ is negligible.

The above results show that the strain stiffening of the DFH architecture in the experimental system is mostly the result of the hyperelastic properties of the matrix, since in this section we show that fiber reorientation in the DFH architecture is constrained by the specific lay-up sequence and therefore strain stiffening is not predicted, which is consistent with the explanation in section 3.3.2 and the analytical prediction in Fig. 4(e). Moreover, we investigate the effect of an elasto-plastic matrix to replace the linear elastic matrix for the DFH architecture with $\theta_h = 30^\circ$, large strains, and found no strain stiffening either, see *section S10*.

4. Concluding remarks

This work examines the mechanical properties of a hybrid architecture, the Discontinuous Fiber Helicoid (DFH), which takes inspiration from a regular helicoid composite and a 'brick and mortar' architecture. The combination of these two motifs gives rise to some unique composite mechanics. Like the regular helicoid, each unidirectional lamina is highly anisotropic due to the alignment of the fibers. However, the elastic behavior of whole helicoidal laminate is transversely isotropic.

The properties of DFH architecture are a function of the geometry and the property of its constituents. Among the dominant geometrical features, we can mention pitch angle, θ_h. Constitutive properties, such as the fiber to matrix stiffness ratio, as well as the matrix nonlinear behavior, are relevant as they relate to strain stiffening and overall failure. To deconvolve the various effects, we examined various architectures, namely DFH/DMB/DSL, to gain insights into the contribution

of deformation to fiber reorientation, $\Delta\theta_c$, as it relates to lamina misorientation with respect to the loading direction and lay-up sequence.

- We found that the DFH architecture exhibits less in-plane shear deformation and less transverse contraction leading to smaller values of fiber reorientation, $\Delta\theta_c$, compared with the DMB and DSL architectures. We compared and quantified $\Delta\theta_c$ in individual laminae from different architectures. For instance, we found that the individual lamina θ_{30} of the DFH $\theta_h = 30^\circ$ exhibits up to 29.5% lower $\Delta\theta_c$ than that found in the DSL $\theta_s = 30^\circ$ upon 15% strain. On the other hand, the θ_{45} lamina in the DMB architecture exhibits 28.6% higher value of $\Delta\theta_c$ than the θ_{45} lamina in the DFH with $\theta_h = 45^\circ$. In fact, the DFH architecture, due to its overall balanced lay-up sequence, exhibits smaller in-plane shear deformation than the DSL architecture and less contraction in the transverse direction than the DMB architecture. The DMB $\theta_b = 30^\circ$ exhibits a 93.4% higher ν_{xy} than the DSL architecture with $\theta_s = 30^\circ$. This is due to its compatible mechanical properties among balanced laminae.
- The analysis reported in this study revealed that the DFH architecture, with a linear elastic or elasto-plastic matrix with small plastic hardening, shows negligible strain stiffening, compared with the DMB architecture, under uniaxial tensile loading, whereas the DMB architecture shows superior strain stiffening compared with DFH architecture (up to 16% under 4% local ε_t and 33.6% under 10% local ε_t). Furthermore, evidence that no strain stiffening is obtained from our FEA results with linear elastic matrix and very small values obtained from plate theory indicates that the strain stiffening observed in 3D printed samples is more likely caused by the anisotropic hyperelastic constitutive response of the matrix.
- Although the DFH architecture and the disorder laminates show the same elastic modulus before deformation, their fiber reorientation and strain stiffening values are slightly different after the same tensile strain (4% local ε_t). This observation confirms that the lay-up sequence influences the deformation in each lamina through the thickness and, thus, has an impact on the fiber reorientation behavior.

In closing, we have provided a rigorous analytical, experimental, and computational analysis of deformation and strain stiffening for a variety of discontinues fiber architectures, which should be valuable for the design of composite materials in which tailoring of constitutive behavior, following some inspiration from these natural materials that can lead to a better mechanical performance. The DFH architecture exhibits some interesting mechanical behaviors, which can be employed in some specific applications. For example, helicoidal composites with compliant matrix and stiffer fibers can find applications where isotropic elastic properties are required under general and relatively low loads, but higher strength and toughness, along the loading direction, under higher loads.

Declaration of competing interest

The authors declare that they have no known competing financial interests or personal relationships that could have appeared to influence the work reported in this paper.

CRediT authorship contribution statement

Di Wang: Conceptualization, Methodology, Software, Validation, Formal analysis, Investigation, Data curation, Writing - original draft, Writing - review & editing, Visualization. **Alireza Zaheri:** Investigation, Resources. **Benjamin Russell:** Conceptualization, Writing - review & editing. **Horacio Espinosa:** Conceptualization, Writing - review & editing, Supervision. **Pablo Zavattieri:** Conceptualization, Writing - review & editing, Supervision, Project administration.

Acknowledgements

The authors wish to acknowledge financial support from the Multi-University Research Initiative (AFOSR-FA9550-15-1-0009). Special thanks to Nicolás Guarín-Zapata for fruitful discussions on some aspects of the model.

Appendix A. Supplementary data

Supplementary data to this article can be found online at https://doi.org/10.1016/j.jmbbm.2020.103914.

References

Barthelat, F., Tang, H., Zavattieri, P.D., Li, C.M., Espinosa, H.D., 2007. On the mechanics of mother-of-pearl: a key feature in the material hierarchical structure. J. Mech. Phys. Solid. https://doi.org/10.1016/j.jmps.2006.07.007.
Barthelat, F., Yin, Z., Buehler, M.J., 2016. Structure and mechanics of interfaces in biological materials. Nat. Rev. Mater. https://doi.org/10.1038/natrevmats.2016.7.
Bigi, A., Burghammer, M., Falconi, R., Koch, M.H.J., Panzavolta, S., Riekel, C., 2001. Twisted plywood pattern of collagen fibrils in teleost scales: an X-ray diffraction investigation. J. Struct. Biol. 136, 137–143. https://doi.org/10.1006/jsbi.2001.4426.
Bouligand, Y., 1972. Twisted fibrous arrangements in biological materials and cholesteric mesophases. Tissue Cell 4, 189–217. https://doi.org/10.1016/S0040-8166(72)80042-9.
Bruet, B.J.F., Song, J., Boyce, M.C., Ortiz, C., 2008. Materials design principles of ancient fisharmour. Nat. Mater. 7, 748–756. https://doi.org/10.1038/nmat2231.
Carlsson, L.A., Adams, D.F., Pipes, R.B., 2014. Experimental characterization of advanced composite materials, experimental characterization of advanced composite materials. https://doi.org/10.1201/b16618.
Chen, P.Y., McKittrick, J., Meyers, M.A., 2012. Biological materials: functional adaptations and bioinspired designs. Prog. Mater. Sci. https://doi.org/10.1016/j.pmatsci.2012.03.001.
Cheng, L., Wang, L., Karlsson, A.M., 2008. Image analyses of two crustacean exoskeletons and implications of the exoskeletal microstructure on the mechanical behavior. J. Mater. Res. 23, 2854–2872. https://doi.org/10.1557/JMR.2008.0375.
Cheng, L., Thomas, A., Glancey, J.L., Karlsson, A.M., 2011. Mechanical behavior of bio-inspired laminated composites. Compos. Part A Appl. Sci. Manuf. 42, 211–220. https://doi.org/10.1016/j.compositesa.2010.11.009.
Chung, W.J., Oh, J.W., Kwak, K., Lee, B.Y., Meyer, J., Wang, E., Hexemer, A., Lee, S.W., 2011. Biomimetic self-templating supramolecular structures. Nature 478, 364–368. https://doi.org/10.1038/nature10513.
Daniel, Isaac M., Ishai, Ori, 1994. Engineering Mechanics of Composite Materials, vol. 3. New York Oxford Univ. Press, 256-256.
de Obaldia, E.E., Jeong, C., Grunenfelder, L.K., Kisailus, D., Zavattieri, P., 2015. Analysis of the mechanical response of biomimetic materials with highly oriented microstructures through 3D printing, mechanical testing and modeling. J. Mech. Behav. Biomed. Mater. 48, 70–85. https://doi.org/10.1016/j.jmbbm.2015.03.026.
Fang, Z., Wang, Y., Feng, Q., Kienzle, A., Müller, W.E.G., 2014. Hierarchical structure and cytocompatibility of fish scales from Carassius auratus. Mater. Sci. Eng. C 43, 145–152. https://doi.org/10.1016/j.msec.2014.07.015.
Gil-Duran, S., Arola, D., Ossa, E.A., 2016. Effect of chemical composition and microstructure on the mechanical behavior of fish scales from Megalops Atlanticus. J. Mech. Behav. Biomed. Mater. 56, 134–145. https://doi.org/10.1016/j.jmbbm.2015.11.028.
Ginzburg, D., Pinto, F., Iervolino, O., Meo, M., 2017. Damage tolerance of bio-inspired helicoidal composites under low velocity impact. Compos. Struct. 161, 187–203. https://doi.org/10.1016/j.compstruct.2016.10.097.
Grunenfelder, L.K., Suksangpanya, N., Salinas, C., Milliron, G., Yaraghi, N., Herrera, S., Evans-Lutterodt, K., Nutt, S.R., Zavattieri, P., Kisailus, D., 2014. Bio-inspired impact-resistant composites. Acta Biomater. 10, 3997–4008. https://doi.org/10.1016/j.actbio.2014.03.022.
Guarín-Zapata, N., Gomez, J., Yaraghi, N., Kisailus, D., Zavattieri, P.D., 2015. Shear wave filtering in naturally-occurring Bouligand structures. Acta Biomater. 23, 11–20. https://doi.org/10.1016/j.actbio.2015.04.039.
Halpin, J.C., 1969. Stiffness and expansion estimates for oriented short fiber composites. J. Compos. Mater. 3, 732–734. https://doi.org/10.1177/002199836900300419.
Hofer, A.K., Walton, R., Ševeček, O., Messing, G.L., Bermejo, R., 2020. Design of damage tolerant and crack-free layered ceramics with textured microstructure. J. Eur. Ceram. Soc. https://doi.org/10.1016/j.jeurceramsoc.2019.09.004.
Ikoma, T., Kobayashi, H., Tanaka, J., Walsh, D., Mann, S., 2003. Microstructure, mechanical, and biomimetic properties of fish scales from Pagrus major. J. Struct. Biol. 142, 327–333. https://doi.org/10.1016/S1047-8477(03)00053-4.
Ji, B., Gao, H., 2004. Mechanical properties of nanostructure of biological materials. J. Mech. Phys. Solid. 52, 1963–1990. https://doi.org/10.1016/j.jmps.2004.03.006.
Kose, O., Tran, A., Lewis, L., Hamad, W.Y., MacLachlan, M.J., 2019. Unwinding a spiral of cellulose nanocrystals for stimuli-responsive stretchable optics. Nat. Commun. 10 https://doi.org/10.1038/s41467-019-08351-6.
Lin, Y.S., Wei, C.T., Olevsky, E.A., Meyers, M.A., 2011. Mechanical properties and the laminate structure of Arapaima gigas scales. J. Mech. Behav. Biomed. Mater. 4, 1145–1156. https://doi.org/10.1016/j.jmbbm.2011.03.024.

Mencattelli, L., Pinho, S.T., 2019. Realising bio-inspired impact damage-tolerant thin-ply CFRP Bouligand structures via promoting diffused sub-critical helicoidal damage. Compos. Sci. Technol. 182, 107684. https://doi.org/10.1016/j.compscitech.2019.107684.

Menig, R., Meyers, M.H., Meyers, M.A., Vecchio, K.S., 2000. Quasi-static and dynamic mechanical response of Haliotis rufescens (abalone) shells. Acta Mater. 48, 2383–2398. https://doi.org/10.1016/S1359-6454(99)00443-7.

Meyers, M.A., Chen, P.-Y., Lin, A.Y.-M., Seki, Y., 2008. Biological materials: structure and mechanical properties. Prog. Mater. Sci. 53, 1–206. https://doi.org/10.1016/j.pmatsci.2007.05.002.

Meyers, M.A., Lin, Y.S., Olevsky, E.A., Chen, P.Y., 2012. Battle in the amazon: Arapaima versus piranha. Adv. Eng. Mater. 14, 279–288. https://doi.org/10.1002/adem.201180027.

Murcia, S., Lavoie, E., Linley, T., Devaraj, A., Ossa, E.A., Arola, D., 2017. The natural armors of fish: a comparison of the lamination pattern and structure of scales. J. Mech. Behav. Biomed. Mater. 73, 17–27. https://doi.org/10.1016/j.jmbbm.2016.09.025.

Porter, M.M., Ravikumar, N., Barthelat, F., Martini, R., 2017. 3D-printing and mechanics of bio-inspired articulated and multi-material structures. J. Mech. Behav. Biomed. Mater. 73, 114–126. https://doi.org/10.1016/j.jmbbm.2016.12.016.

Quan, H., Yang, W., Schaible, E., Ritchie, R.O., Meyers, M.A., 2018. Novel defense mechanisms in the armor of the scales of the "living fossil" coelacanth fish. Adv. Funct. Mater. 28 https://doi.org/10.1002/adfm.201804237.

Raabe, D., Romano, P., Sachs, C., Al-Sawalmih, A., Brokmeier, H.G., Yi, S.B., Servos, G., Hartwig, H.G., 2005. Discovery of a honeycomb structure in the twisted plywood patterns of fibrous biological nanocomposite tissue. J. Cryst. Growth 283, 1–7. https://doi.org/10.1016/j.jcrysgro.2005.05.077.

Ramirez, G., 1999. Book reviews: design and optimization of laminated composite materials. J. Struct. Eng. 125 https://doi.org/10.1061/(asce)0733-9445(1999)125:9(1082), 1082–1082.

Reddy, J.N., 2013. An Introduction to Continuum Mechanics, Second Edition, an Introduction to Continuum Mechanics, second ed. https://doi.org/10.1017/cbo9781139178952

Rivlin, R.S., Saunders, D.W., 1951. Large elastic deformations of isotropic materials. VII. Experiments on the deformation of rubber. Philos. Trans. R. Soc. A Math. Phys. Eng. Sci. 243, 251–288. https://doi.org/10.1098/rsta.1951.0004.

Roland, J.C., Reis, D., Vian, B., Roy, S., 1989. The helicoidal plant cell wall as a performing cellulose-based composite. Biol. Cell 67, 209–220. https://doi.org/10.1111/j.1768-322X.1989.tb00864.x.

Sachs, C., Fabritius, H., Raabe, D., 2008. Influence of microstructure on deformation anisotropy of mineralized cuticle from the lobster Homarus americanus. J. Struct. Biol. 161, 120–132. https://doi.org/10.1016/j.jsb.2007.09.022.

Sakhavand, N., Shahsavari, R., 2015. Universal composition-structure-property maps for natural and biomimetic platelet-matrix composites and stacked heterostructures. Nat. Commun. 6 https://doi.org/10.1038/ncomms7523.

Salinas, C., Kisailus, D., 2013. Fracture mitigation strategies in gastropod shells. JOM (J. Occup. Med.) 65, 473–480. https://doi.org/10.1007/s11837-013-0570-y.

Shishehbor, M., Zavattieri, P.D., 2019. Effects of interface properties on the mechanical properties of bio-inspired cellulose nanocrystal (CNC)-based materials. J. Mech. Phys. Solid. 124, 871–896. https://doi.org/10.1016/j.jmps.2018.12.002.

Stratasys Ltd, 2018. Stratasys Vero material data sheet [WWW Document]. URL. https://www.stratasys.com/materials/search/vero.

Stratasys Ltd, 2019. Stratasys tango datasheet [WWW Document]. Strat. Tango Datasheet. URL. https://www.stratasys.com/materials/search/tango.

Studart, A.R., 2016. Additive manufacturing of biologically-inspired materials. Chem. Soc. Rev. https://doi.org/10.1039/c5cs00836k.

Suksangpanya, N., Yaraghi, N.A., Kisailus, D., Zavattieri, P., 2017. Twisting cracks in Bouligand structures. J. Mech. Behav. Biomed. Mater. 76, 38–57. https://doi.org/10.1016/j.jmbbm.2017.06.010.

Suksangpanya, N., Yaraghi, N.A., Pipes, R.B., Kisailus, D., Zavattieri, P., 2018. Crack twisting and toughening strategies in Bouligand architectures. Int. J. Solid Struct. 150, 83–106. https://doi.org/10.1016/j.ijsolstr.2018.06.004.

Sun, J., Bhushan, B., 2012. Hierarchical structure and mechanical properties of nacre: a review. RSC Adv. 2, 7617–7632. https://doi.org/10.1039/c2ra20218b.

Torres, F.G., Troncoso, O.P., Nakamatsu, J., Grande, C.J., Gómez, C.M., 2008. Characterization of the nanocomposite laminate structure occurring in fish scales from Arapaima Gigas. Mater. Sci. Eng. C 28, 1276–1283. https://doi.org/10.1016/j.msec.2007.12.001.

Tucker, C.L., Liang, E., 1999. Stiffness predictions for unidirectional short-fiber composites: review and evaluation. Compos. Sci. Technol. 59, 655–671. https://doi.org/10.1016/S0266-3538(98)00120-1.

Weaver, J.C., Milliron, G.W., Miserez, A., Evans-Lutterodt, K., Herrera, S., Gallana, I., Mershon, W.J., Swanson, B., Zavattieri, P., DiMasi, E., Kisailus, D., 2012. The stomatopod dactyl club: a formidable damage-tolerant biological hammer. Science 336, 1275–1280. https://doi.org/10.1126/science.1218764 (80-.).

Wei, X., Naraghi, M., Espinosa, H.D., 2012. Optimal length scales emerging from shear load transfer in natural materials: application to carbon-based nanocomposite design. ACS Nano 6, 2333–2344. https://doi.org/10.1021/nn204506d.

Yang, W., Sherman, V.R., Gludovatz, B., Mackey, M., Zimmermann, E.A., Chang, E.H., Schaible, E., Qin, Z., Buehler, M.J., Ritchie, R.O., Meyers, M.A., 2014. Protective role of Arapaima gigas fish scales: structure and mechanical behavior. Acta Biomater. 10, 3599–3614. https://doi.org/10.1016/j.actbio.2014.04.009.

Yang, W., Liu, Q., Yue, Z., Li, X., Xu, B., 2017. Rotation of hard particles in a soft matrix. J. Mech. Phys. Solid. 101, 285–310. https://doi.org/10.1016/j.jmps.2017.01.008.

Yang, W., Quan, H., Meyers, M.A., Ritchie, R.O., 2019. Arapaima fish scale: one of the toughest flexible biological materials. SSRN Electron. J. 1–10 https://doi.org/10.2139/ssrn.3401845.

Yao, H., Zheng, G., Li, W., McDowell, M.T., Seh, Z., Liu, N., Lu, Z., Cui, Y., 2013. Crab shells as sustainable templates from nature for nanostructured battery electrodes. Nano Lett. 13, 3385–3390. https://doi.org/10.1021/nl401729r.

Yin, S., Yang, W., Kwon, J., Wat, A., Meyers, M.A., Ritchie, R.O., 2019. Hyperelastic phase-field fracture mechanics modeling of the toughening induced by Bouligand structures in natural materials. J. Mech. Phys. Solid. 131, 204–220. https://doi.org/10.1016/j.jmps.2019.07.001.

Zaheri, A., Fenner, J.S., Russell, B.P., Restrepo, D., Daly, M., Wang, D., Hayashi, C., Meyers, M.A., Zavattieri, P.D., Espinosa, H.D., 2018. Revealing the mechanics of helicoidal composites through additive manufacturing and beetle developmental stage analysis. Adv. Funct. Mater. 28 https://doi.org/10.1002/adfm.201803073.

Zelazny, B., Neville, A.C., 1972. Quantitative studies on fibril orientation in beetle endocuticle. J. Insect Physiol. 18 https://doi.org/10.1016/0022-1910(72)90243-0.

Zhang, Z.Q., Liu, B., Huang, Y., Hwang, K.C., Gao, H., 2010. Mechanical properties of unidirectional nanocomposites with non-uniformly or randomly staggered platelet distribution. J. Mech. Phys. Solid. 58, 1646–1660. https://doi.org/10.1016/j.jmps.2010.07.004.

Zhang, P., Heyne, M.A., To, A.C., 2015. Biomimetic staggered composites with highly enhanced energy dissipation: modeling, 3D printing, and testing. J. Mech. Phys. Solid. 83, 285–300. https://doi.org/10.1016/j.jmps.2015.06.015.

Zhang, C., Mcadams, D.A., Grunlan, J.C., 2016. Nano/micro-manufacturing of bioinspired materials: a review of methods to mimic natural structures. Adv. Mater. https://doi.org/10.1002/adma.201505555.

Zhu, D., Ortega, C.F., Motamedi, R., Szewciw, L., Vernerey, F., Barthelat, F., 2012. Structure and mechanical performance of a "modern" fish scale. Adv. Eng. Mater. 14, 185–194. https://doi.org/10.1002/adem.201180057.

Zimmermann, E.A., Gludovatz, B., Schaible, E., Dave, N.K.N., Yang, W., Meyers, M.A., Ritchie, R.O., 2013. Mechanical adaptability of the Bouligand-type structure in natural dermal armour. Nat. Commun. 4, 1–7. https://doi.org/10.1038/ncomms3634.